

# Cross-Modality Controlled Molecule Generation with Diffusion Language Model

Yunzhe Zhang<sup>1</sup>, Yifei Wang<sup>1</sup>, Khanh Vinh Nguyen<sup>1</sup>, Pengyu Hong<sup>1\*</sup>

<sup>1</sup>Brandeis University, Waltham, MA, USA

{yunzhezhang, yifeiwang, andrewng, hongpeng}@brandeis.edu

## Abstract

Current SMILES-based diffusion models for molecule generation typically support only unimodal constraint. They inject conditioning signals at the start of the training process and require retraining a new model from scratch whenever the constraint changes. However, real-world applications often involve multiple constraints across different modalities, and additional constraints may emerge over the course of a study. This raises a challenge: how to extend a pre-trained diffusion model not only to support cross-modality constraints but also to incorporate new ones without retraining. To tackle this problem, we propose the Cross-Modality Controlled Molecule Generation with Diffusion Language Model (CMCM-DLM), demonstrated by two distinct cross modalities: molecular structure and chemical properties. Our approach builds upon a pre-trained diffusion model, incorporating two trainable modules, the Structure Control Module (SCM) and the Property Control Module (PCM), and operates in two distinct phases during the generation process. In Phase I, we employ the SCM to inject structural constraints during the early diffusion steps, effectively anchoring the molecular backbone. Phase II builds on this by further introducing PCM to guide the later stages of inference to refine the generated molecules, ensuring their chemical properties match the specified targets. Experimental results on multiple datasets demonstrate the efficiency and adaptability of our approach, highlighting CMCM-DLM's significant advancement in molecular generation for drug discovery applications.

## Introduction

Drug discovery is essential for developing new therapeutic treatments, aiming to identify molecules, within a vast chemical space, with desirable properties such as drug-likeness, lipophilicity, and synthetic accessibility. Traditional methods are labor-intensive, time-consuming, and heavily reliant on domain expertise, rendering the process costly and inefficient (Hughes et al. 2011). Recent advances in artificial intelligence (AI) have revolutionized this field by introducing data-driven techniques that more effectively explore the chemical space (Gómez-Bombarelli et al. 2018). AI-based methods, including deep learning and reinforcement learning, can predict molecular properties, optimize

structures, and accelerate drug design, significantly reducing both time and cost (Zhavoronkov et al. 2019; Schneider et al. 2020). These advances are pivotal for personalized medicine, improving treatment efficacy, and enabling the development of therapeutics for complex diseases (Lavecchia 2015).

Recently, diffusion models (Ho, Jain, and Abbeel 2020; Song, Meng, and Ermon 2021) have emerged as powerful generative models, excelling in image generation and outperforming GANs. These models produce high-quality images by denoising random noise through learning to estimate the score function of the data distribution, allowing diverse outputs with minimal supervision (Song et al. 2021). Moreover, their ability to control properties such as style, content, and composition makes them ideal for tasks that require precise guidance (Rombach et al. 2022). Recent improvements, including classifier-free and classifier-based guidance (Ho and Salimans 2022a; Dhariwal and Nichol 2021), enhance the controllability of diffusion generation through the integration of explicit or implicit classifiers, offering great potential for molecule generation under different constraints to advance drug discovery.

Current molecule generation methods often rely on SMILES representations (Weininger 1988; Weininger, Weininger, and Weininger 1989), which encode molecular structures as ASCII strings, making them suitable for integration into machine learning models. Specifically, one popular approach conditions the generation process on textual descriptions, training models to produce molecules matching specified inputs and enabling greater control over outputs (Gong et al. 2024). In contrast, a more advanced method introduces a chemically informative latent space, combined with data augmentation and contrastive learning, to better align generated molecules with textual prompts and improve generation performance (Wang et al. 2024).

However, these approaches face two major challenges. First, integrating conditions throughout the entire training leads to inefficiency, as even minor changes in the dataset or conditions require retraining the model from scratch. Second, text-guided generation is inherently limited to one single structural modality, which does not meet the demands of drug discovery. In this context, effective drug design demands not only cross-modality control that simultaneously addresses structural fidelity and property optimization, but

\*Corresponding author

Copyright © 2026, Association for the Advancement of Artificial Intelligence (www.aaai.org). All rights reserved.

also enables large pre-trained diffusion language models to flexibly adapt to multifaceted generative objectives.

To address the aforementioned limitations, we propose Cross-Modality Controlled Molecule Generation with Diffusion Language Model (**CMCM-DLM**), an efficient and flexible approach that proceeds in a two-phase generation process. In Phase I, the Structure Control Module is applied using classifier-free guidance to condition the early diffusion steps on structural information, effectively anchoring the molecular backbone. In Phase II, we introduce a Property Control Module that collaborates with SCM, using classifier-based guidance from pretrained property predictors to steer generation toward desired chemical properties while maintaining structural constraints. By decoupling structural and property control across two diffusion stages, CMCM-DLM enables scalable and cross-modality molecule generation. As illustrated in Figure 1, CMCM-DLM integrates multiple guidance signals during inference and offers the following practical benefits:

- **Plug-and-Play.** By training only the SCM and PCM, the CMCM-DLM enables controllable generation on any frozen pretrained model without re-training, simply by plugging in the modules at inference.
- **Flexible.** The property and structure control modules support a wide range of constraints, including chemical properties such as QED, PLogP, and SAS, as well as diverse scaffold types for enforcing structural constraints.
- **Composable.** Different combinations of property and structural constraints can be composed to enable various forms of cross-modality control.
- **Lightweight Training.** The structure module requires less than one-fifth of the pre-training time for fine-tuning, while the property module takes no more than half, effectively enabling fast adaptation to new constraints.

Our contributions are summarized as follows: (1) We are the first to combine classifier-based and classifier-free guidance for cross-modality constrained generation of SMILES molecules using diffusion language model. Our approach integrates cross-modality control directly into the inference process, enabling efficient and flexible molecule generation. Empirically, our method achieves an average scaffold similarity of 55% and improves target property satisfaction by 16% across three benchmark datasets. (2) The Property Control Module independently enables the simultaneous optimization of multiple molecular properties, achieving an average relative improvement of 52% over dataset means. This highlights its ability to balance complex property trade-offs beyond the reach of previous methods. (3) The Structure Control Module, in contrast, focuses on precise scaffold regulation with minimal fine-tuning, reaching an average structure adherence of 70% while preserving high validity, novelty, and diversity. Its efficiency makes it particularly suitable for fast, structure-constrained generation tasks.

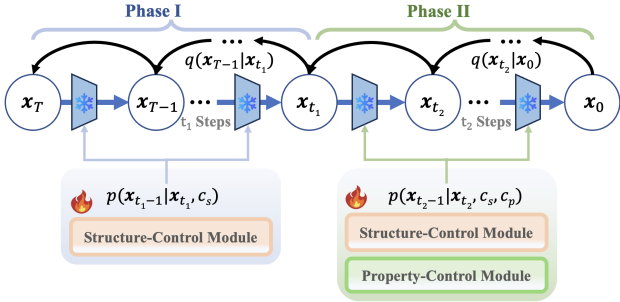


Figure 1: Our CMCM-DLM method guides SMILES-based molecular generation using a pre-trained diffusion model without retraining. It operates in two phases: Phase I incorporates structural constraints  $c_s$  to guide generation based on structure information; Phase II applies cross-modality constraints ( $c_s, c_p$ ) to refine the process with both structural and property guidance. These constraints are efficiently injected into the reverse diffusion process as  $p(x_t | x_{t+1}, c_s, c_p)$ .

## Related Works

### SMILES-based molecule generation

Molecules can be represented in various forms, such as SMILES strings, molecular graphs (Guo et al. 2022), or 3D structures (Chen et al. 2023; Zhu et al. 2022), with SMILES receiving significant attention due to its simplicity and efficiency. Traditional methods, including recurrent neural networks (RNNs) and variational autoencoders (VAEs), have been used to generate valid and novel SMILES strings. For example, an RNN-based approach (Segler et al. 2018) generates SMILES step-by-step using one-hot encoding and a probabilistic language model, while the VAE-based GVAE (Kusner, Paige, and Hernández-Lobato 2017) introduces grammar-based constraints to ensure syntactic validity and chemical plausibility. Advances in deep learning have also enabled the development of auto-regressive models, which are particularly well-suited for string-based tasks like SMILES generation. Notable examples include GPT (Floridi and Chiriaci 2020), which has demonstrated strong performance in language modeling. Building on this foundation, ChemGPT (Frey et al. 2022) and MolGPT (Bagal et al. 2021) adapt the GPT framework for molecular generation. More recently, diffusion models have emerged as a promising alternative. For instance, Text-Guided Molecule Generation with Diffusion Language Model (Gong et al. 2024) is the first to apply diffusion models to SMILES generation. However, unlike prior work that focuses solely on generating valid, novel, and diverse SMILES, our approach enables cross-modality controllable generation, allowing the discovery of optimal molecules for drug discovery.

### Controllable molecules generation

Controllable molecule generation has emerged as a key approach for addressing challenges in drug discovery and material design, enabling precise tuning of molecular properties to meet specific requirements. To this end, graph-based

methods enforce scaffold substructures to emphasize structural control (Lim et al. 2020), while GPT-based models like MolGPT focus on property optimization (Bagal et al. 2021). In parallel, the rise of diffusion models and classifier-free guidance (Ho and Salimans 2022b) has spurred interest in text-conditioned molecular generation. For example, TGM-DLM (Gong et al. 2024) pioneered the use of diffusion language models to align molecules with text descriptions. Building on this, LDMol (Wang et al. 2024) tackles the discreteness of SMILES via a latent diffusion framework combined with contrastive learning. Additionally, Equivariant Diffusion (Hoogeboom et al. 2022) enables efficient 3D molecular structure generation while preserving geometric constraints. Despite these advances, the joint control of structure and property across modalities remains underexplored. In this work, we systematically explore cross-modality controllable generation and demonstrate its effectiveness in addressing the challenges of joint structural and property control.

## Preliminary and Task Formulation

This section outlines the preliminaries of the key components of molecular generation pipeline using diffusion language model for SMILES generation, adapted from (Li et al. 2022; Gong et al. 2024).

### Pre-diffusion

**Data Augmentation.** During training, we enhance input data by replacing a molecule’s SMILES string with its equivalent representation using RDKit inspired by (Schwaller et al. 2019). This improves novelty and diversity in the generation process based on a probability threshold.

**Encoding and Embedding.** To apply the continuous diffusion model, the discrete SMILES string must be embedded into a continuous representation. We first used Chem-Char Tokenizer with vocabulary size  $v$  maps each SMILES token to a one-hot vector. An embedding layer within the prediction model then projects these vectors into  $d$ -dimensional continuous representations. For a SMILES string of length  $n$ , the resulting embedding lies in  $\mathbb{R}^{nd}$ .

### After-diffusion

**Decoding and Rounding.** The backward diffusion process produces  $x_0 \in \mathbb{R}^{nd}$ , representing a molecule with  $n$  tokens. Each column of  $x_0$  is then mapped to the nearest one-hot vector using L2 distance. Then these one-hot vectors are decoded into their corresponding chemical elements using Chem-Char Tokenizer, effectively reconstructing a SMILES string from  $x_0$ .

### Diffusion model

A diffusion model mainly contains two processes: forward and backward diffusion.

**Forward process.** Given the prior continuous data distribution  $x_0 \sim q(x_0)$ , the number of diffusion steps  $T$ , and a variance scheduler  $\alpha_t$ , a forward process gradually transforms the input into pure Gaussian noise  $x_T \sim \mathcal{N}(0, \mathbf{I})$ ,

with transitions defined as follows:

$$\begin{aligned} q(x_{1:T} | x_0) &:= \prod_{t=1}^T q(x_t | x_{t-1}) \\ q(x_t | x_{t-1}) &:= \mathcal{N}(x_t; \sqrt{\alpha_t}x_{t-1}, (1 - \alpha_t)\mathbf{I}) \end{aligned} \quad (1)$$

where  $\alpha_t = 1 - \beta_t$ , and  $\beta_t$  is a predefined variance schedule that controls the noise level at each diffusion step  $t$ . During the forward diffusion process, Gaussian noise is gradually injected at each step, such that the sample  $x_T$  approximates a standard normal distribution  $\mathcal{N}(0, \mathbf{I})$ .

**Backward process.** This process starts from a noisy sample  $x_T \sim \mathcal{N}(0, \mathbf{I})$ , denoises  $x_t$  to generate  $x_{t-1}$  at each step, and finally produces a clean sample  $x_0$  with total  $T$  steps. Instead of predicting  $x_{t-1}$  from  $x_t$ , a Transformer-based model  $\epsilon_\theta$  is trained to directly predict  $x_0$  from  $x_t$  to improve denoising accuracy. Then the denoising transition from  $x_t$  to  $x_{t-1}$  is reformulated as:

$$\begin{aligned} x_{t-1} \sim \mathcal{N} \left( x_{t-1}; \frac{\sqrt{\alpha_{t-1}}\beta_t}{1 - \bar{\alpha}_t} \epsilon(x_t, t; \theta) \right. \\ \left. + \frac{\sqrt{\alpha_t}(1 - \bar{\alpha}_{t-1})}{1 - \bar{\alpha}_t} x_t, \frac{1 - \bar{\alpha}_{t-1}}{1 - \bar{\alpha}_t} \beta_t \mathbf{I} \right) \end{aligned} \quad (2)$$

where given a noisy  $x_T$ , we sequentially apply Equation 2 to sample  $x_{t-1}$ , eventually producing  $x_0$ , which is then converted into a SMILES string by the After-diffusion process.

## Method

Our CMCM-DLM method, shown in Figure 2, employs two trainable control modules, SCM and PCM, to guide a frozen pre-trained diffusion model through two phases of inference. Phase I uses only SCM to enforce structural constraints, while Phase II uses both modules to generate molecules with desired structures and improved chemical properties.

### Phase I: Single Modality Control

Rather than generating molecules purely from noise, Phase I of CMCM-DLM begins from  $x_T \sim \mathcal{N}(0, \mathbf{I})$  and incorporates structural information by using only the SCM to guide the generation process. We denote any timestep in this phase by  $t_1$ , the diffusion state at that timestep by  $x'_{t_1}$ , and the structure constraints as  $c_s$ . Then the prediction model  $\epsilon(x_t, t; \theta)$  in Equation 2 is replaced with the structure-guided variant  $\tilde{\epsilon}_s(x'_{t_1}, t_1, c_s; \theta_s)$ , reflecting its role in Phase I.

Our SCM is inspired by T2I Adapter (Mou et al. 2023) and ControlNet (Zhang, Rao, and Agrawala 2023), which enable text-guided image synthesis by fine-tuning only newly added components to adapt to new conditions such as styles or prompts, while keeping the pre-trained diffusion model weights frozen to maintain generation quality. This design supports efficient adaptation to new conditions without full retraining. Similarly, our SCM adopts this strategy to integrate structural constraints into molecular generation.

In practice, users define the structural constraint  $s$  via scaffold that captures the core structure of the desired molecules and is applied consistently throughout the reverse

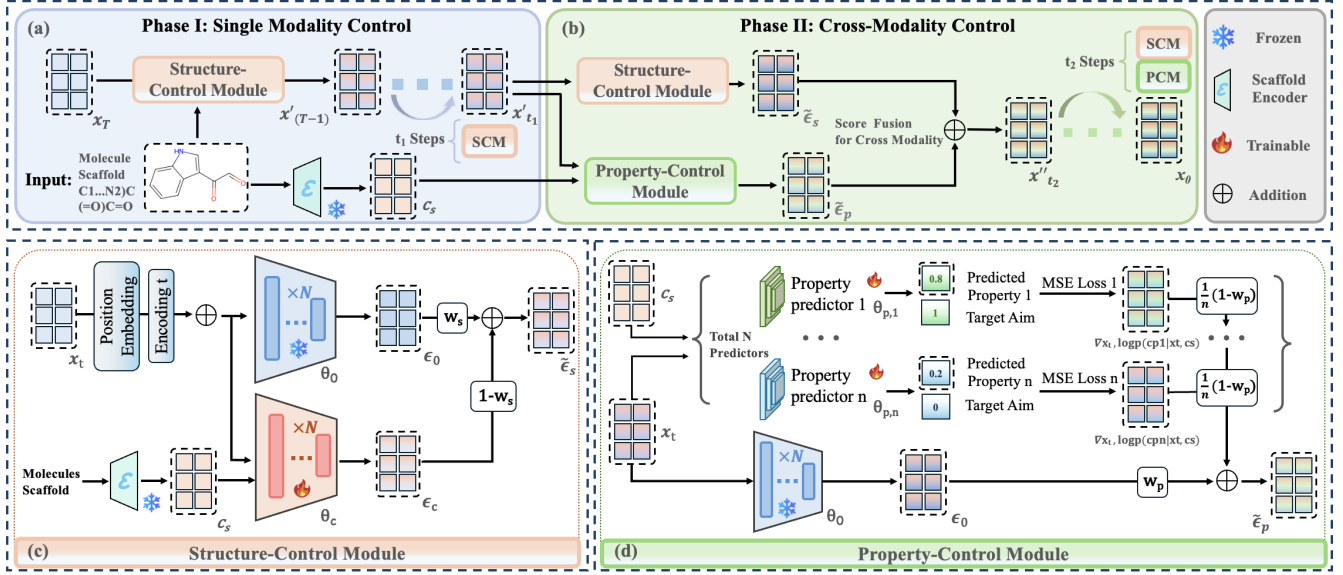


Figure 2: CMCM-DLM consists of two phases shown in the upper part as (a) and (b). Phase I performs single-modality control using SCM, while Phase II enables cross-modality control by incorporating SCM and PCM. The lower part shows the internal architectures of SCM (c) and PCM (d) based on the provided parameters.

diffusion process. In our implementation, scaffolds are encoded as SMILES strings and transformed into latent embeddings  $c_s \in \mathbb{R}^{d \times m}$  using a frozen pre-trained scaffold encoder (Sun et al. 2024), where  $d$  is the embedding dimension and  $m$  is the scaffold length. The SCM employs classifier-free guidance (Ho and Salimans 2022b) to balance conditional and unconditional guided prediction, as defined by:

$$\tilde{\epsilon}_s(x'_{t_1}, t_1, c_s; \theta_s) = w_s \cdot \epsilon(x'_{t_1}, t_1; \theta_0) + (1 - w_s) \cdot \epsilon(x'_{t_1}, t_1, c_s; \theta_c) \quad (3)$$

here,  $\tilde{\epsilon}_s$  denotes the structure-guided prediction produced by the SCM, with  $\theta_s = \theta_0 \cup \theta_c$ . The parameter set  $\theta_0$  corresponds to the frozen unconditional prediction model, while  $\theta_c$  comprises newly introduced parameters for encoding structural information. The weight  $w_s$  controls the contribution of each component and the detailed architecture of the SCM is provided in the Appendix Section B.

The frozen unconditional prediction model  $\epsilon(x'_{t_1}, t_1; \theta_0)$  operates at each diffusion step  $t_1$  as follows. The noisy embedding  $x'_{t_1}$  is concatenated with the timestep encoding and positional embeddings to form  $z_{t_1}^{(0)}$ , which serves as the input to the first layer. Each subsequent layer  $z_{t_1}^{(i+1)}$  in the  $N$ -layer network is then computed as:

$$\begin{aligned} z'_{t_1}^{(i)} &= \text{LN}_{\theta_0}(z_{t_1}^{(i)} + \text{SelfAttention}_{\theta_0}(z_{t_1}^{(i)})) \\ z_{t_1}^{(i+1)} &= \text{LN}_{\theta_0}(z_{t_1}^{(i)} + \text{DP}_{\theta_0}(\text{FFN}_{\theta_0}(z_{t_1}^{(i)}))) \end{aligned} \quad (4)$$

where LN represents layer normalization, FFN is feed-forward network, and DP is the dropout layer.

Similarly, we design  $\epsilon(x'_{t_1}, t_1, c_s; \theta_c)$  by extending a trainable version of  $\epsilon(x'_{t_1}, t_1; \theta_0)$  with a cross-attention module

to incorporate the structural constraint  $c_s$ . Notably,  $Z_{t_1}^{(i)}$  denotes the input to the  $i$ -th layer of the trainable model and serves to distinguish it from the frozen model in Equation 4, while the initial input  $Z_{t_1}^{(0)}$  remains identical to  $z_{t_1}^{(0)}$ . Each layer is computed as follows:

$$\begin{aligned} Z'_{t_1}^{(i)} &= \text{LN}_{\theta_c}(Z_{t_1}^{(i)} + \text{SelfAttention}_{\theta_c}(Z_{t_1}^{(i)})) \\ &+ \text{Cross-Attention}_{\theta_c}(\text{SelfAttention}_{\theta_c}(Z_{t_1}^{(i)}), c_s) \\ Z_{t_1}^{(i+1)} &= \text{LN}_{\theta_c}(Z_{t_1}^{(i)} + \text{DP}_{\theta_c}(\text{FFN}_{\theta_c}(Z_{t_1}^{(i)}))) \end{aligned} \quad (5)$$

Lastly, the outputs  $z_{t_1}^{(N)}$  from the frozen Transformer  $\epsilon(x'_{t_1}, t_1; \theta_0)$  and  $Z_{t_1}^{(N)}$  from the trainable Transformer  $\epsilon(x'_{t_1}, t_1, c_s; \theta_c)$  are combined via Equation 3 to produce the structure-guided prediction  $\tilde{\epsilon}_s(x'_{t_1}, t_1, c_s; \theta_s)$ .

## Phase II: Cross-Modality Control

**Score Fusion for Cross-Modality Control.** Following the Phase I diffusion process, the resulting early state  $x'_{t_1}$  already captures a basic molecular structure due to the injected structural information. However, structure alone may not ensure desirable properties, highlighting the need for Phase II Cross-Modality Control. Phase II proceeds from the final state of Phase I to  $x_0$ . We denote any timestep in this phase by  $t_2$ , the diffusion state at that timestep by  $x''_{t_2}$ , and the structural and property conditions as  $c_s$  and  $c_p$ , respectively. The standard prediction model  $\epsilon(x_t, t; \theta)$  in Equation 2 is replaced with the cross-modality variant  $\tilde{\epsilon}(x''_{t_2}, t_2, c_s, c_p; \theta_s, \theta_p)$ , which jointly incorporates both structural and property guidance.

To achieve cross-modality control that incorporates both  $c_s$  and  $c_p$  conditions, we reinterpret the conditional distribution  $p(x_t | t, c_s, c_p)$  as estimating a joint conditional score

that reflects both modalities. Following score-based diffusion modeling (Song et al. 2021), the prediction network  $\epsilon(x_t, t, c; \theta)$  parameterized the gradient of the log of the target conditional distribution, which we refer to as the conditional score. Thus, in Phase II, we approximate this conditional target distribution by combining two conditional scores derived from separately conditioned prediction models, one guided by  $c_s$ , and the other by  $\mathbf{c}_p$ . Each predicts a modality-specific score component, and their outputs are additively fused to guide the denoising process. Then the final prediction is computed as:

$$\begin{aligned}\tilde{\epsilon}(x''_{t_2}, t_2, c_s, \mathbf{c}_p; \theta_s, \theta_p) &= \tilde{\epsilon}_s(x''_{t_2}, t_2, c_s; \theta_s) \\ &+ \tilde{\epsilon}_p(x''_{t_2}, t_2, c_s, \mathbf{c}_p; \theta_p),\end{aligned}\quad (6)$$

here, we additionally introduce the PCM to compute the property-guided prediction  $\tilde{\epsilon}_p(x''_{t_2}, t_2, c_s, \mathbf{c}_p; \theta_p)$ , while  $\tilde{\epsilon}_s(x''_{t_2}, t_2, c_s; \theta_s)$  denotes the structure-guided prediction produced by the same SCM used in Phase I. A detailed proof of Equation 6 is provided in the Appendix Section F.

**Property Control Module** The Property Control Module (PCM) guides the generation of molecules toward desired chemical properties by injecting property-specific signals into the reverse diffusion process, while simultaneously enforcing the structural constraint  $c_s$ . Although traditional classifier-free guidance can be effective in certain settings, it often lacks the precision and specificity needed to reliably steer molecular generation toward target property profiles.

To address this, we adopt classifier-based guidance (Dhariwal and Nichol 2021) to improve the chemical properties of generated molecules. As most chemical properties are continuous rather than categorical, we train a property prediction model  $p(\mathbf{c}_p | x''_{t_2}, t_2, c_s; \theta_p)$ , where  $\theta_p$  denotes the model parameters. The vector  $\mathbf{c}_p = \{c_{p,1}, c_{p,2}, \dots, c_{p,n}\}$  represents  $n$  target properties, such as drug-likeness, solubility, and hydrophobicity. To guide generation toward desired property values while capturing inter-property dependencies and respecting structural constraints, we modify  $\tilde{\epsilon}_p(x''_{t_2}, t_2, c_s, \mathbf{c}_p; \theta_p)$  as follows:

$$\begin{aligned}\tilde{\epsilon}_p(x''_{t_2}, t_2, c_s, \mathbf{c}_p; \theta_p) &= w_p \epsilon(x''_{t_2}, t_2; \theta_0) + \\ &(1 - w_p) \sum_{i=1}^n \nabla_{x''_{t_2}} \log p(c_{p,i} | x''_{t_2}, t_2, c_s, \mathbf{c}_{p \setminus i}; \theta_{p,i})\end{aligned}\quad (7)$$

where  $\tilde{\epsilon}_p$  denotes the property-guided prediction produced by the PCM, and  $\theta_p$  includes all PCM parameters: the frozen pre-trained Transformer  $\theta_0$  and a property predictor  $p_i$  with parameters  $\theta_{p,i}$ . The weight  $w_p$  controls the influence of the property predictor, balancing the unconditional score and property-specific guidance. Additionally,  $\mathbf{c}_{p \setminus i} = \{c_{p,1}, \dots, c_{p,i-1}, c_{p,i+1}, \dots, c_{p,n}\}$  denotes all property conditions excluding  $c_{p,i}$ .

Specifically, during Phase II, we apply Langevin dynamics by back propagating the loss through the noisy SMILES representation, iteratively refining the latent variables to optimize the desired chemical properties. For a single property  $c_{p,i}$ , the set  $\mathbf{c}_{p \setminus i}$  is empty, as no other property constraints are applied. If structural constraints are absent, the condition  $c_s$  is omitted during single-property enhancement.

## Training

For simplicity, we use  $x_t$  to denote the diffusion state and  $t$  as the timestep in this section.

**Training the property control module.** We train a Transformer-based property predictor with 12 layers and 12 attention heads. The input  $x_t$  is generated by sampling molecules from the dataset, mapping into embeddings using a pre-trained model, and adding  $t$ -step noise to simulate the diffusion process. When structural constraints are also applied, the scaffold is incorporated via cross-attention to account for its effect on property prediction. The model is optimized using mean squared error (MSE) between predicted and ground truth property values:

$$\mathcal{L}_1 = \mathbb{E}_{x_t \sim \text{Noise\_EMB}(x_0)} \left[ \left\| \sum_{i=1}^n p(c_{p,i} | x_t, t, \mathbf{c}_{p \setminus i}, c_s; \theta_p) - c_{\text{true}} \right\|^2 \right] \quad (8)$$

where  $c_{\text{true}}$  represents the corresponding ground truth of  $c_{p,i}$ .

**Training the structure control module.** We designed the following objective function  $\mathcal{L}_2(x_t, c_s)$  to replace the original loss function, which requires reconstructing  $x_0$  at each backward diffusion step under the structure constraint  $c_s$ :

$$\begin{aligned}\mathcal{L}_2(x, c_s) = \mathbb{E}_{q(x_{0:T} | M)} \left[ \sum_{t=1}^T \left\| \epsilon(x_t, t, c_s; \theta_s) - x_0 \right\|^2 \right. \\ \left. - \log r_\theta(x | x_0) \right]\end{aligned}\quad (9)$$

where  $r_\theta(x | x_0)$  denotes the rounding process described in After-diffusion section.

## Inference

The backward diffusion in CMCM-DLM starts from Gaussian noise and is guided in two phases: Phase I applies only structural constraints, as molecular structures are unclear in early steps and Phase II incorporates both structural and property guidance. We test different transition timesteps  $t_1$  and  $t_2$  to separate the two phases. Besides, we set  $w_s = 1 - w_p$  for consistency in Equation 6, and the inference algorithm is provided in the Appendix Section C.

## Experiments

We first evaluated the performance of the CMCM-DLM under cross-modality constraints and then we separately investigated the influence of PCM and the effectiveness of SCM.

## Experimental setup

**Datasets:** To comprehensively evaluate our model, we conducted experiments on three widely used molecular datasets: GuacaMol, ZINC250K, and QM9. GuacaMol, derived from the ChEMBL 24 database (Mendez et al. 2019), contains 1.6 million bio-active molecules with diverse properties and serves as a benchmark for testing generative models under property constraints. ZINC250K (Irwin et al. 2012) includes 249455 drug-like molecules (up to 38 atoms) across

Dataset	Method	Basic		Property			Structure	
		Validity $\uparrow$	Novelty $\uparrow$	QED $\uparrow$	SAS $\downarrow$	PlogP $\uparrow$	Improvement (%) $\uparrow$	Scaffold Similarity (%) $\uparrow$
GuacaMol	CMCM-DLM <sub>QED</sub>	80%	100%	0.71	2.61	-7.89	[34%]	51%
	CMCM-DLM <sub>SAS</sub>	86%	97%	0.67	2.02	-6.69	[27%]	55%
	CMCM-DLM <sub>PlogP</sub>	90%	99%	0.53	2.10	-5.42	[22%]	60%
	CMCM-DLM <sub>QED+SAS</sub>	83%	98%	0.70	2.22	-7.24	[33%, 20%]	52%
	CMCM-DLM <sub>QED+PlogP</sub>	82%	100%	0.69	2.30	-6.80	[30%, 2%]	52%
	CMCM-DLM <sub>SAS+PlogP</sub>	82%	98%	0.67	2.13	-6.69	[24%, 8%]	53%
	CMCM-DLM <sub>QED+SAS+PlogP</sub>	80%	98%	0.69	2.12	-6.73	[30%, 24%, 5%]	52%
Zinc	CMCM-DLM <sub>QED</sub>	92%	98%	0.78	2.83	-6.32	[13%]	48%
	CMCM-DLM <sub>SAS</sub>	93%	93%	0.62	2.32	-4.43	[19%]	53%
	CMCM-DLM <sub>PlogP</sub>	84%	99%	0.56	2.41	-4.12	[11%]	61%
	CMCM-DLM <sub>QED+SAS</sub>	88%	97%	0.75	2.45	-5.31	[8%, 15%]	57%
	CMCM-DLM <sub>QED+PlogP</sub>	84%	100%	0.73	2.52	-4.28	[6%, 7%]	44%
	CMCM-DLM <sub>SAS+PlogP</sub>	91%	98%	0.56	2.39	-4.14	[17%, 10%]	56%
	CMCM-DLM <sub>QED+SAS+PlogP</sub>	81%	98%	0.73	2.42	-4.21	[6%, 16%, 9%]	54%
QM9	CMCM-DLM <sub>QED</sub>	82%	99%	0.62	3.13	-3.21	[24%]	61%
	CMCM-DLM <sub>SAS</sub>	81%	98%	0.51	2.46	-2.39	[18%]	54%
	CMCM-DLM <sub>PlogP</sub>	78%	98%	0.46	2.72	-0.75	[15%]	60%
	CMCM-DLM <sub>QED+SAS</sub>	85%	99%	0.61	2.52	-2.89	[22%, 16%]	63%
	CMCM-DLM <sub>QED+PlogP</sub>	74%	100%	0.57	2.93	-0.82	[14%, 7%]	56%
	CMCM-DLM <sub>SAS+PlogP</sub>	83%	99%	0.49	2.51	-0.76	[16%, 13%]	64%
	CMCM-DLM <sub>QED+SAS+PlogP</sub>	80%	94%	0.56	2.54	-0.85	[12%, 15%, 3%]	48%

Table 1: Evaluation of molecules generated by CMCM-DLM on the GuacaMol dataset under various property (QED, SAS, PlogP) and scaffold constraints. “Improvement (%)” is  $(m_a - m_b)/m_b \times 100$ , where  $m_a$  and  $m_b$  denote the mean property values of generated and training molecules respectively that contain the given scaffold.

9 classes. Molecules are kekulized with RDKit (Landrum et al. 2013), hydrogen atoms removed, and contain single, double, or triple bonds. QM9 (Ramakrishnan et al. 2014) consists of 133885 small organic molecules ( $\leq 9$  heavy atoms: C, H, O, N, F) with quantum chemical properties computed via density functional theory (DFT), and is widely used for property prediction and generation benchmarks. **Evaluation:** The generated molecules were evaluated using three core metrics: validity, novelty, and diversity. Validity is the percentage of chemically valid molecules, assessed with RDKit (Landrum et al. 2013). Novelty measures the fraction of valid molecules not in the training set, reflecting generative originality. Diversity assesses uniqueness among valid molecules, indicating sample variability.

Secondly, we evaluated molecular properties with QED, SAS, and PLogP. Specifically, QED (Bickerton et al. 2012) scores drug-likeness on a 0–1 scale, SAS (Ertl and Schuffenhauer 2009) measures synthetic accessibility from 1 (easy) to 10 (difficult), and PLogP combines lipophilicity (LogP), synthetic accessibility (SAS), and ring complexity into a single drug-likeness metric (see Appendix Section E for concrete definition details).

Lastly, we assessed scaffold fidelity using two metrics: scaffold existence and scaffold similarity. Scaffold existence is determined via RDKit’s HasSubstructMatch, which checks whether a generated molecule contains the target scaffold. Scaffold similarity quantifies structural resemblance by computing the cosine similarity (0–1) between MACCS key fingerprints of the molecule and the scaffold (Durant et al. 2002).

## Cross-Modality Performance of CMCM-DLM

We evaluated various combinations of cross-modality constraints using diffusion language models pretrained on different datasets. Specifically, each SCM was trained on

the same dataset as its corresponding pre-trained diffusion model, whereas the PCM were all trained on the Guacamol dataset. For every constraint setting, 10,000 molecules were generated, and, after removing duplicates, the resulting molecules were assessed using validity, novelty, QED, SAS, PLogP, scaffold similarity, and scaffold existence.

We selected 10 common scaffolds (e.g., pyridine, imidazole) as the Validation Scaffold Set (see Appendix Section G for details), which appear in an average of 17.6% of molecules in pretrained datasets. These scaffolds were combined with three property optimization objectives: QED, SAS, and PLogP, resulting in seven cross-modality constraint combinations. This setup was designed to evaluate the efficiency and adaptability of CMCM-DLM in generating molecules that simultaneously satisfy structural and property-based constraints.

The results in Table 1 clearly show significant improvements of CMCM-DLM across various scenarios. Whether optimizing a single property or combining multiple simultaneously, CMCM-DLM consistently delivers remarkable gains. The novelty of the generated molecules reaches almost 100%. Property improvements reach up to 34%, while structural similarity is and scaffold existence is maintained at 50+% and 70+% in average. When QED, SAS, and PlogP are optimized together, all three metrics improve concurrently, with QED and SAS achieving 17% gains in average while preserving high scaffold existence and similarity.

When multiple cross-modality constraints overlap, inevitable trade-offs arise, particularly between QED and PLogP. Under equal predictor weights  $w_p$  in the PCM, joint optimization of QED, SAS, and PLogP leads to an approximate 16% improvement in QED, while PLogP increases by only 6%. Increasing the weight assigned to the PLogP predictor boosts PLogP gains to around 12%, but QED improvements diminish to approximately 8%. This tension

Molecule	Scaffold	CMCM-DLM <sub>QED+SAS+PLOGP</sub>	CMCM-DLM <sub>QED+SAS</sub>	CMCM-DLM <sub>QED+PLOGP</sub>	CMCM-DLM <sub>SAS+PLOGP</sub>
SMILE String	<chem>c1ccc2nesc2c1</chem>	<chem>CCCC(=O)Nc1nc2cccc2s1</chem>	<chem>COCCNC(=O)c1nc2cc(C)cc(C)c2s1</chem>	<chem>CC(C)(C)CCNC(=O)c1nc2ccc(C)cc2s1</chem>	<chem>CCCCCCCCCCCCC(C)=ONc1nc2cccc2s1</chem>
QED ( $\uparrow$ )	0.5	0.863 ✓	0.862 ✓	0.927 ✓	0.393
SAS ( $\downarrow$ )	2.66	1.716 ✓	2.310 ✓	2.228 ✓	1.918 ✓
PLOGP ( $\uparrow$ )	-6.36	-5.783 ✓	-6.928	-6.012 ✓	-3.888 ✓
Scaffold Similarity ( $\uparrow$ )	-	0.663	0.606	0.640	0.626

Table 2: An optimization example from the Guacamol dataset. The first column shows the scaffold, followed by the optimized molecules generated by CMCM-DLM under different property control combinations: QED+SAS+PlogP, QED+SAS, QED+PlogP, and SAS+PlogP. A check mark (✓) indicates improvement over the scaffold baseline, which is calculated as the mean property scores of all Guacamol molecules containing that scaffold. The property scores (QED ( $\uparrow$ ), SAS ( $\downarrow$ ), PlogP ( $\uparrow$ )) and scaffold similarity are used to evaluate constraint satisfaction and optimization quality. The gray dashed rectangle highlights the location of the retained scaffold.

reflects the inherent opposition between these objectives, QED favors a balanced physicochemical profile, including a moderate logP range, whereas PLogP drives toward higher lipophilicity, often pushing logP beyond QED’s optimal window. Furthermore, scaffold constraints limit structural changes (e.g., addition of hydrophobic groups) that typically enhance PLogP, contributing to its relatively modest improvement in Table 1. In the absence of scaffold constraints, PLogP can increase by up to 47% in single-objective optimization and still shows an average improvement of 29% when optimized alongside other objectives (see Appendix Section D for detailed results). Despite these trade-offs, all constraint settings yield measurable progress, underscoring CMCM-DLM’s ability to balance competing objectives while preserving scaffold fidelity.

## Influence of PCM

We validated the effectiveness of PCM on single- and multi-property optimization tasks using the Guacamol dataset. Our framework improves properties by about 52% while maintaining high molecule quality, novelty and diversity near 100%, and validity around 90%. Besides QED, SAS, and PLogP, we also tested HBA and HBD, which lack inherent optimization direction, and found their values can still be effectively controlled (see Appendix Section D). For benchmarking, we compared against state-of-the-art methods on QED optimization using the ZINC dataset (Table 3). Our framework consistently outperformed competitors across ranking thresholds, achieving top scores of 0.9481 (Top-1), 0.9467 (Top-5), 0.9458 (Top-10), 0.9413 (Top-100), and 0.9189 (Top-1000), establishing a new benchmark in QED optimization.

## Effectiveness of SCM

We evaluated SCM without PCM on the Validation set and further assessed its generalization using five unseen scaffolds from SAMOA (Langevin et al. 2020) as zero-shot samples. On the VS set, scaffold similarity remains steady at 60%, with scaffold existence rising to 80%–90% during training. For zero-shot scaffolds, similarity improves to

Method	QED $\uparrow$				
	Top-1	Top-5	Top-10	Top-100	Top-1000
GraphNVP	0.8512	0.8391	0.8260	0.7423	0.5046
GraphAF	0.9437	0.9261	0.9176	0.8593	0.5749
GDSS	0.9449	0.9369	0.9337	0.9126	0.8512
MoFlow	0.9261	0.9233	0.9150	0.8664	0.7839
D2L-OMP	0.9476	0.9417	0.9372	0.9144	0.8529
<b>MMCD (ours)</b>	<b>0.9481</b>	<b>0.9467</b>	<b>0.9458</b>	<b>0.9413</b>	<b>0.9189</b>

Table 3: Comparison of QED scores for the top-k molecules out of 10,000 generated candidates. Results of GraphNVP, GraphAF, GDSS, and MoFlow are adapted from (Guo, Guan, and Zhou 2023).

80%–86%, and existence reaches 59%, indicating strong generalization. SCM also ensures high molecule quality, with 86% validity, nearly 100% novelty, and approximately 80% diversity across both settings. Notably, it achieves strong results within five epochs, using under 20% of the training time required by full diffusion models, demonstrating high efficiency and practicality.

## Conclusion

The proposed CMCM-DLM framework provides plug-and-play adaptability, supports flexible and composable cross-modality constraints, and enables efficient two-stage training. In Phase I, the Structure Control Module (SCM) enforces structural constraints during the initial diffusion steps to anchor the molecular backbone. In Phase II, guidance scores from both the Property Control Module (PCM) and SCM are integrated to steer the later diffusion process, ensuring the generated molecules satisfy specified chemical property targets. Experimental results on three different dataset demonstrate that CMCM-DLM effectively reconciles conflicting cross-modality constraints, achieving an average improvement of 16% in property metrics while maintaining approximately 79% structural fidelity, establishing a new benchmark for diffusion-based molecular generation under cross-modality constraints.

## References

Bagal, V.; Aggarwal, R.; Vinod, P.; and Priyakumar, U. D. 2021. MolGPT: molecular generation using a transformer-decoder model. *Journal of Chemical Information and Modeling*, 62(9): 2064–2076.

Bickerton, G. R.; Paolini, G. V.; Besnard, J.; Muresan, S.; and Hopkins, A. L. 2012. Quantifying the chemical beauty of drugs. *Nature chemistry*, 4(2): 90–98.

Chen, D.; Zhu, Y.; Zhang, J.; Du, Y.; Li, Z.; Liu, Q.; Wu, S.; and Wang, L. 2023. Uncovering Neural Scaling Laws in Molecular Representation Learning. *arXiv preprint arXiv:2309.15123*.

Dhariwal, P.; and Nichol, A. 2021. Diffusion models beat gans on image synthesis. *Advances in neural information processing systems*, 34: 8780–8794.

Durant, J. L.; Leland, B. A.; Henry, D. R.; and Nourse, J. G. 2002. Reoptimization of MDL keys for use in drug discovery. *Journal of Chemical Information and Computer Sciences*, 42(6): 1273–1280.

Ertl, P.; and Schuffenhauer, A. 2009. Estimation of synthetic accessibility score of drug-like molecules based on molecular complexity and fragment contributions. *Journal of Cheminformatics*, 1(1): 8.

Floridi, L.; and Chiriatti, M. 2020. GPT-3: Its nature, scope, limits, and consequences. *Minds and Machines*, 30(4): 681–694.

Frey, N.; Soklaski, R.; Axelrod, S.; Samsi, S.; Gomez-Bombarelli, R.; Coley, C.; and Gadepally, V. 2022. Neural scaling of deep chemical models. *arXiv preprint arXiv:2204.09624*.

Gómez-Bombarelli, R.; Wei, J. N.; Duvenaud, D.; Hernández-Lobato, J. M.; Sanchez-Lengeling, B.; Sheberla, D.; Aguilera-Iparraguirre, J.; Hirzel, T. D.; Adams, R. P.; and Aspuru-Guzik, A. 2018. Automatic Chemical Design Using a Data-Driven Continuous Representation of Molecules. *ACS Central Science*, 4(2): 268–276.

Gong, H.; Liu, Q.; Wu, S.; and Wang, L. 2024. Text-Guided Molecule Generation with Diffusion Language Model. *arXiv preprint arXiv:2402.13040*.

Guo, S.; Guan, J.; and Zhou, S. 2023. Diffusing on Two Levels and Optimizing for Multiple Properties: A Novel Approach to Generating Molecules with Desirable Properties. *arXiv preprint arXiv:2303.54321*.

Guo, Z.; Guo, K.; Nan, B.; Tian, Y.; Iyer, R. G.; Ma, Y.; Wiest, O.; Zhang, X.; Wang, W.; Zhang, C.; and Chawla, N. V. 2022. Graph-based Molecular Representation Learning. *arXiv preprint arXiv:2207.04869*.

Ho, J.; Jain, A.; and Abbeel, P. 2020. Denoising diffusion probabilistic models. *arXiv preprint arXiv:2006.11239*.

Ho, J.; and Salimans, T. 2022a. Classifier-free diffusion guidance. *arXiv preprint arXiv:2207.12598*.

Ho, J.; and Salimans, T. 2022b. Classifier-Free Diffusion Guidance. *arXiv preprint arXiv:2207.12598*. {jonathanho, salimans}@google.com.

Hoogeboom, E.; Satorras, V. G.; Vignac, C.; and Welling, M. 2022. Equivariant diffusion for molecule generation in 3D. *arXiv preprint arXiv:2203.17003*.

Hughes, J. D.; Rees, S.; Kalindjian, S. B.; and Philpott, K. L. 2011. Principles of early drug discovery. *British journal of pharmacology*, 162(6): 1239–1249.

Irwin, J. J.; Sterling, T.; Mysinger, M. M.; Bolstad, E. S.; and Coleman, R. G. 2012. ZINC: a free tool to discover chemistry for biology. *Journal of Chemical Information and Modeling*, 52(7): 1757–1768.

Kingma, D. P.; and Ba, J. 2015. Adam: A Method for Stochastic Optimization. In *Proceedings of the 3rd International Conference on Learning Representations (ICLR 2015), Conference Track Proceedings*. San Diego, CA, USA.

Kusner, M. J.; Paige, B.; and Hernández-Lobato, J. M. 2017. Grammar variational autoencoder. In *International Conference on Machine Learning*, 1945–1954. PMLR.

Landrum, G.; et al. 2013. RDKit: A software suite for cheminformatics, computational chemistry, and predictive modeling. *Greg Landrum*, 8(31.10): 5281.

Langevin, M.; Minoux, H.; Levesque, M.; and Bianciotto, M. 2020. Scaffold-constrained molecular generation. *arXiv preprint arXiv:2009.07778*.

Lavecchia, A. 2015. Machine-learning approaches in drug discovery: methods and applications. *Drug discovery today*, 20(3): 318–331.

Li, X.; Thickstun, J.; Gulrajani, I.; Liang, P. S.; and Hashimoto, T. B. 2022. Diffusion-lm improves controllable text generation. *Advances in Neural Information Processing Systems*, 35: 4328–4343.

Lim, J.; Hwang, S.-Y.; Moon, S.; Kim, S.; and Kim, W. Y. 2020. Scaffold-based molecular design with a graph generative model. *Chemical Science*, 11: 1153–1164.

Mendez, D.; Gaulton, A.; Bento, A. P.; Chambers, J.; De Veij, M.; Félix, E.; Magariños, M. P.; Mosquera, J. F.; Mutowo, P.; Nowotka, M.; et al. 2019. ChEMBL: towards direct deposition of bioassay data. *Nucleic acids research*, 47(D1): D930–D940.

Mou, L.; Shi, Z.; Cui, Y.; Liu, S.; Jiang, Y.; Zhang, B.; and Wang, Y. 2023. T2I-Adapter: Learning Adapters to Dig out More Controllable Ability for Text-to-Image Diffusion Models. *arXiv preprint arXiv:2302.08453*.

Ramakrishnan, R.; Dral, P. O.; Rupp, M.; and von Lilienfeld, O. A. 2014. Quantum chemistry structures and properties of 134 kilo molecules. *Scientific Data*, 1: 140022.

Rombach, R.; Blattmann, A.; Lorenz, D.; Esser, P.; and Ommer, B. 2022. High-Resolution Image Synthesis with Latent Diffusion Models. In *Proceedings of the IEEE/CVF Conference on Computer Vision and Pattern Recognition*, 10684–10695.

Schneider, P.; Walters, W. P.; Plowright, A. T.; Sieroka, N.; Listgarten, J.; Goodnow, R. A.; Fisher, J.; Jansen, J. M.; Duca, J. S.; Rush, T. S.; et al. 2020. Deep learning in drug discovery: machine learning in drug design. *Journal of medicinal chemistry*, 63(16): 8705–8722.

Schwaller, P.; Laino, T.; Gaudin, T.; Bolgar, P.; Hunter, C. A.; Bekas, C.; and Lee, A. A. 2019. Molecular Transformer: A Model for Uncertainty-Calibrated Chemical Reaction Prediction. *ACS Central Science*, 5(9): 1572–1583.

Segler, M. H. S.; Kogej, T.; Tyrchan, C.; and Waller, M. P. 2018. Generating focused molecule libraries for drug discovery with recurrent neural networks. *ACS Central Science*, 4(1): 120–131.

Song, J.; Meng, C.; and Ermon, S. 2021. Denoising Diffusion Implicit Models. In *International Conference on Learning Representations (ICLR)*.

Song, Y.; Sohl-Dickstein, J.; Kingma, D. P.; Kumar, A.; Ermon, S.; and Poole, B. 2021. Score-based generative modeling through stochastic differential equations. In *International Conference on Learning Representations*. ICLR.

Sun, H.; Xue, X.; Liu, X.; Hu, H.-Y.; Deng, Y.; and Wang, X. 2024. Cross-Modal Retrieval Between  $^{13}\text{C}$  NMR Spectra and Structures Based on Focused Libraries. *Analytical Chemistry*, 96(6): 1234–1242.

Wang, L.; Xu, J.; Li, S.; et al. 2024. LDMol: Text-Conditioned Molecule Diffusion Model Leveraging Chemically Informative Latent Space. *arXiv preprint arXiv:2405.17829*.

Weininger, D. 1988. SMILES, a chemical language and information system. 1. Introduction to methodology and encoding rules. *Journal of chemical information and computer sciences*, 28(1): 31–36.

Weininger, D.; Weininger, A.; and Weininger, J. L. 1989. SMILES. 2. Algorithm for generation of unique SMILES notation. *Journal of Chemical Information and Computer Sciences*, 29(2): 97–101.

Zhang, L.; Rao, A.; and Agrawala, M. 2023. Adding Conditional Control to Text-to-Image Diffusion Models. *arXiv preprint arXiv:2302.05543*.

Zhavoronkov, A.; Ivanenkov, Y. A.; Aliper, A.; Veselov, M. S.; Aladinskiy, V. A.; Aladinskaya, A. V.; Terentiev, V. A.; Polykovskiy, D. A.; Kuznetsov, M. D.; Asadulaev, A.; et al. 2019. Artificial intelligence for drug discovery, biomarker development, and generation of novel chemistry. *Nature reviews Drug discovery*, 18(1): 41–57.

Zhu, Y.; Chen, D.; Du, Y.; Wang, Y.; Liu, Q.; and Wu, S. 2022. Featurizations matter: a multiview contrastive learning approach to molecular pretraining. In *ICML 2022 2nd AI for Science Workshop*.

## Technical Appendix

### A: Implementation Details

In this section, we describe the implementation details of the training for SCM and PCM. All experiments are done on the NVIDIA V100 32GB.

#### Training Details for the Pre-trained Diffusion Model

The maximum sequence length for tokenized SMILES strings was set to  $n = 100$ . A character-level tokenizer tailored for chemical structures, with a vocabulary size of 590, was used. The Transformer model  $\epsilon(x_t, t; \theta_0)$  was configured with  $N = 12$  layers, 12 attention heads, and a hidden dimension of  $d = 768$ . An augmentation level of 0.8 was applied, and training was performed over 2000 diffusion steps. The model comprises approximately 87 million trainable parameters.

Pre-training was carried out using the Adam optimizer (Kingma and Ba 2015) with a learning rate of  $1 \times 10^{-4}$ . The training spanned seven days across three datasets, covering a total of 800,000 epochs. The resulting model  $\epsilon(x_t, t; \theta_0)$  serves as the backbone for SMILES generation in the subsequent SCM and PCM training phases.

**Training Details for PCM** For PCM training, diffusion steps beyond 1500 were excluded due to the absence of well-defined molecular structures in this range, as observed during preliminary experiments. Consequently, property prediction was focused on diffusion steps below 1500. A Transformer-based property predictor was employed, consisting of 12 encoder layers, 12 attention heads, and a hidden dimension of 768. When integrated with SCM, scaffold information  $c_s$  was incorporated via a cross-attention mechanism. In contrast, property-only enhancement omitted scaffold integration.

Training was conducted using the Adam optimizer, with learning rates ranging from  $1 \times 10^{-5}$  to  $1 \times 10^{-4}$ , depending on the specific property being optimized. Generally, higher diffusion steps required smaller learning rates to maintain training stability. For diffusion steps in the range of 0–1000, training typically converged within one day, while steps between 1000 and 1500 required approximately three days to reach stability and effectiveness.

In addition to QED, SAS, and PLogP, we evaluated the controllability of other chemical properties such as LogP, HBA, and more. The expected control performance was achieved; however, as these properties lack inherent directional biases, detailed results are omitted. Furthermore, we observed that setting excessively high target values for properties often resulted in a noticeable decline in the validity of generated molecules, although it led to a marked improvement in the target property itself.

**Training Details for SCM** For SCM training, the pre-trained scaffold encoder was configured with a hidden dimension of  $d = 768$ . The SCM prediction model consists of two components: the pre-trained model  $\epsilon(x_t, t; \theta_0)$  and the scaffold-conditioned model  $\tilde{\epsilon}(x_t, t, c_s; \theta_c)$ . The latter shares the same architecture as  $\epsilon(x_t, t; \theta_0)$ , including 12 layers and 12 attention heads, but introduces an additional

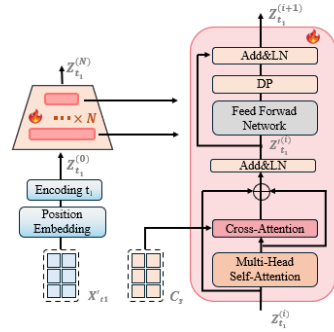


Figure 3: Visualization of the architecture for the newly added trainable copy Transformer  $\tilde{\epsilon}(x_t, t, c_s; \theta_c)$ .

cross-attention mechanism at each layer to incorporate scaffold information. The detailed architecture is provided in Section B.

The SCM model was fine-tuned briefly, inheriting all training settings from the pre-training phase, including the optimizer, warm-up strategy, learning rate schedule, and other hyperparameters.

### B: Architecture of SCM

The detailed architecture of  $\tilde{\epsilon}(x_t, t, c_s; \theta_c)$  within SCM is illustrated in Figure 3. The input  $x_t$  is first combined with the corresponding timestep encoding and positional embedding to construct the initial representation. The computation performed at each layer of the  $N$ -layer network is shown in right side of Figure 3. After propagating through all  $N$  layers, the final output  $Z_{t_1}^{(N)}$  represents the model prediction  $\tilde{\epsilon}(x_t, t, c_s; \theta_c)$ .

### C: Inference of CMCM-DLM

The inference process of CMCM-DLM is divided into two distinct phases, as illustrated in Figure 2 of the main paper, with the corresponding algorithm detailed in Algorithm 1. Sampling begins from Gaussian noise, and different denoising equations are applied to estimate  $x_{t-1}$  from  $x_t$ , depending on the conditioning used in each phase. We experimented with various total step configurations for both Phase I and Phase II. In all experiments reported in this paper, we set the weighting factors  $w_p = w_s = 0.5$ , with the timestep  $t_1$  decreasing from 2000 to 1500 in Phase I and  $t_2$  continuing from 1500 to 0 in Phase II.

Moreover, we observed that the balance between structural fidelity and property optimization during inference is highly sensitive to the weighting factor  $w_s$ . A larger  $w_s$  places greater emphasis on structural consistency, significantly improving structure-related metrics while limiting gains in property optimization. In contrast, a smaller  $w_s$  enhances property-related metrics at the cost of reduced structural quality. Furthermore, setting the Phase II timestep

range  $t_2$  to span the full interval from 0 to 1500 yields substantially better property optimization. Any shorter range with an upper bound below 1500 (e.g.,  $t_2 = 0$  to 1000) consistently results in inferior property-related performance.

#### Algorithm 1: Reversing inference process of CMCM-DLM

```

1: Sample  $x'_T \sim \mathcal{N}(0, I)$ 
2: for  $t_1 \leftarrow T$  to  $t_2$  do ▷ Phase One
3:   Obtain  $\tilde{\epsilon}_s$  using Eq. (3)
4:   Sample  $z \sim \mathcal{N}(0, I)$ 
5:    $x'_{t_1-1} = \frac{\sqrt{\alpha_{t_1-1}}\beta_{t_1}}{1-\alpha_{t_1}}\tilde{\epsilon}_s + \frac{\sqrt{\alpha_{t_1}}(1-\alpha_{t_1-1})}{1-\alpha_{t_1}}x'_{t_1} + \sigma_{t_1}z$ 
6: for  $t_2$  to 1 do ▷ Phase Two
7:   Obtain  $\tilde{\epsilon}_s$  using Eq. (3)
8:   Obtain  $\tilde{\epsilon}_p$  using Eq. (7)
9:   if  $t_2 > 1$  then Sample  $z \sim \mathcal{N}(0, I)$  else  $z \leftarrow 0$ 
10:   $\tilde{\epsilon} \leftarrow \tilde{\epsilon}_s + \tilde{\epsilon}_p$ 
11:   $x''_{t_2-1} = \frac{\sqrt{\alpha_{t_2-1}}\beta_{t_2}}{1-\alpha_{t_2}}\tilde{\epsilon} + \frac{\sqrt{\alpha_{t_2}}(1-\alpha_{t_2-1})}{1-\alpha_{t_2}}x''_{t_2} + \sigma_{t_2}z$ 
Ensure:  $x_0$ 

```

## D: Further Experiments Results

**SCM Results** To further validate the effectiveness of SCM, we visualize in Figure 4 the evolution of structural alignment throughout the training process. Specifically, the figure illustrates how scaffold similarity and scaffold existence progressively improve as SCM adapts the generative model to better match target scaffolds. During training, scaffold existence in the validation set steadily increases from 80% to 90%, while scaffold similarity remains consistently around 60%. Notably, for zero-shot scaffolds, those unseen during training, a clear upward trend in scaffold similarity is observed, reaching 80%–86%. These results demonstrate that SCM effectively enhances structural alignment between generated molecules and desired scaffolds over time, and more importantly, generalizes well beyond the training distribution.

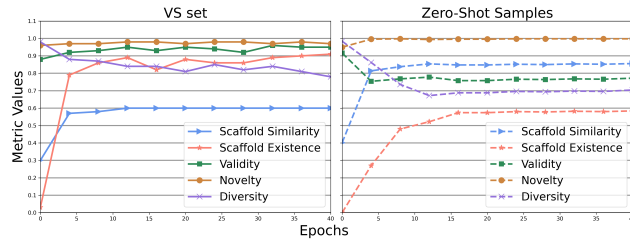


Figure 4: Visualization of basic metrics and structure metrics as the SCM’s training progresses. The left plot corresponds to the VS set, while the right plot corresponds to 5 selected zero-shot scaffolds.

**PCM Results** To further evaluate the effectiveness and flexibility of the standalone PCM module (without SCM), we conducted additional experiments focusing on its ability to optimize molecular properties in the absence of structure

constraints. In particular, we tested PCM’s capability to both increase and decrease the values of HBA and HBD, which differ from properties like QED, SAS, and PLogP due to their lack of a clear directional optimization objective. As shown in Table 4, PCM achieves an average improvement of 96% when increasing HBA and HBD, and 83% when decreasing them. These results demonstrate PCM’s strong controllability across undirected properties. Given the absence of a defined optimization direction, HBA and HBD were excluded from the cross-modality experiments evaluating CMCM-DLM’s overall performance.

Method	Guacamol			
	Validity $\uparrow$	Novelty $\uparrow$	Diversity $\uparrow$	Improvement $\uparrow$
Property <sub>QED</sub>	86%	99%	100%	[58%]
Property <sub>SAS</sub>	88%	96%	99%	[26%]
Property <sub>PlogP</sub>	82%	99%	90%	[47%]
Property <sub>HBA+</sub>	66%	100%	100%	[67%]
Property <sub>HBA-</sub>	87%	97%	95%	[74%]
Property <sub>HBD+</sub>	93%	98%	97%	[142%]
Property <sub>HBD-</sub>	91%	98%	99%	[91%]
Property <sub>QED+SAS</sub>	91%	98%	98%	[56%, 25%]
Property <sub>QED+PlogP</sub>	93%	98%	97%	[44%, 19%]
Property <sub>SAS+PlogP</sub>	83%	99%	91%	[35%, 49%]
Property <sub>QED+SAS+PlogP</sub>	93%	98%	97%	[44%, 31%, 18%]

Table 4: The performance of the PCM was evaluated for single or combined property optimization, where the symbols + and – indicate whether the optimization aims to increase or decrease the HBA and HBD property values, respectively. The Improvement (%) measures the percentage increase in the mean property values of generated molecules compared to the dataset mean, reflecting their proportional difference.

## E: PLogP Definition

PLogP is a composite metric that can be defined in various ways, depending on the context and objectives of molecular evaluation. In this work, we define PLogP as a combination of three components: the LogP (partition coefficient), synthetic accessibility (SAS), and a cycle size penalty. LogP measures the hydrophobicity of a molecule and is crucial for assessing properties like solubility and membrane permeability. The synthetic accessibility reflects the ease of synthesizing a molecule, with lower values indicating higher synthetic feasibility. The cycle size penalty accounts for the presence of large rings, penalizing molecules with rings larger than six atoms while ignoring smaller rings. To ensure consistency and comparability, all components are normalized using the mean ( $\mu$ ) and standard deviation ( $\sigma$ ) values derived from the dataset. The normalization process rescales each term to have zero mean and unit variance. The PLogP formula is expressed as:

$$\begin{aligned}
 \text{PLogP} = & \frac{\text{LogP} - \mu_{\text{LogP}}}{\sigma_{\text{LogP}}} + \frac{\text{SAS} - \mu_{\text{SAS}}}{\sigma_{\text{SAS}}} \\
 & + \frac{\text{Cycle Penalty} - \mu_{\text{Cycle}}}{\sigma_{\text{Cycle}}}
 \end{aligned} \tag{10}$$

## F:Proof of Equation (6)

**Proof:** We begin with the conditional distribution  $p(x_t|t, c_s, \mathbf{c}_p)$ , which represents the target distribution constrained by both structural ( $c_s$ ) and property ( $\mathbf{c}_p$ ) conditions. By applying the chain rule of probability, we can express it as:

$$p(x_t|t, c_s, \mathbf{c}_p) \propto p(x_t|t) p(c_s, \mathbf{c}_p|x_t, t)$$

Taking the logarithm of both sides yields:

$$\log p(x_t|t, c_s, \mathbf{c}_p) \propto \log p(x_t|t) + \log p(c_s, \mathbf{c}_p|x_t, t)$$

Assuming the conditional independence of  $c_s$  and  $\mathbf{c}_p$ , and introducing parameters  $w$  and  $1-w$  to balance their respective contributions, we further decompose  $p(c_s, \mathbf{c}_p|x_t, t)$  as follows:

$$\log p(c_s, \mathbf{c}_p|x_t, t) = w \log p(c_s|x_t, t) + (1-w) \log p(\mathbf{c}_p|x_t, t, c_s)$$

Substituting this back, we obtain:

$$\begin{aligned} \log p(x_t|t, c_s, \mathbf{c}_p) &\propto \log p(x_t|t) \\ &\quad + w \log p(c_s|x_t, t) \\ &\quad + (1-w) \log p(\mathbf{c}_p|x_t, t, c_s) \end{aligned} \quad (11)$$

To compute the gradient with respect to  $x_t$ , we differentiate both sides:

$$\begin{aligned} \nabla_{x_t} \log p(x_t|t, c_s, \mathbf{c}_p) &= \nabla_{x_t} \log p(x_t|t) \\ &\quad + w \nabla_{x_t} \log p(c_s|x_t, t) \\ &\quad + (1-w) \nabla_{x_t} \log p(\mathbf{c}_p|x_t, t, c_s) \end{aligned} \quad (12)$$

Decomposing  $\nabla_{x_t} \log p(x_t|t)$ , we have:

$$\begin{aligned} \nabla_{x_t} \log p(x_t|t, c_s, \mathbf{c}_p) &= (1-w+w) \nabla_{x_t} \log p(x_t|t) \\ &\quad + w \nabla_{x_t} \log p(c_s|x_t, t) \\ &\quad + (1-w) \nabla_{x_t} \log p(\mathbf{c}_p|x_t, t, c_s) \end{aligned} \quad (13)$$

Reorganizing terms, this becomes:

$$\begin{aligned} \nabla_{x_t} \log p(x_t|t, c_s, \mathbf{c}_p) &= w \nabla_{x_t} \log p(x_t|t) \\ &\quad + (1-w) \nabla_{x_t} \log p(\mathbf{c}_p|x_t, t, c_s) \\ &\quad + (1-w) \nabla_{x_t} \log p(x_t|t) \\ &\quad + w \nabla_{x_t} \log p(c_s|x_t, t) \end{aligned} \quad (14)$$

Assuming we set  $w_p = w$  to balance the property condition module (PCM) contributions and  $w_s = 1-w = 1-w_p$  for the structural condition module (SCM) contributions, we rewrite the equation as:

$$\begin{aligned} \nabla_{x_t} \log p(x_t|t, c_s, \mathbf{c}_p) &= w_p \nabla_{x_t} \log p(x_t|t) \\ &\quad + (1-w_p) \nabla_{x_t} \log p(\mathbf{c}_p|x_t, t, c_s) \\ &\quad + w_s \nabla_{x_t} \log p(x_t|t) \\ &\quad + (1-w_s) \nabla_{x_t} \log p(c_s|x_t, t) \end{aligned} \quad (15)$$

The diffusion score is defined as  $\epsilon(x_t, t, c) \approx \nabla_{x_t} \log p(x_t|t, c)$  and  $\epsilon(x_t, t) \approx \nabla_{x_t} \log p(x_t|t)$ . Considering the parameters  $\theta_s$ ,  $\theta_p$ , and  $\theta_0$ , we have the following expressions:

$$\tilde{\epsilon}(x_t, t, c_s, \mathbf{c}_p; \theta_s, \theta_p) \approx \nabla_{x_t} \log p(x_t|t, c_s, \mathbf{c}_p)$$

$$\epsilon(x_t, t, \theta_0) \approx \nabla_{x_t} \log p(x_t|t).$$

Substituting these terms, we have:

$$\begin{aligned} \tilde{\epsilon}(x_t, t, c_s, \mathbf{c}_p; \theta_s, \theta_p) &\approx w_p \epsilon(x_t, t, \theta_0) \\ &\quad + (1-w_p) \nabla_{x_t} \log p(\mathbf{c}_p|x_t, t, c_s) \\ &\quad + w_s \nabla_{x_t} \log p(x_t|t) \\ &\quad + (1-w_s) \nabla_{x_t} \log p(c_s|x_t, t) \end{aligned} \quad (16)$$

The term  $\nabla_{x_t} \log p(\mathbf{c}_p|x_t, t, c_s)$  actually represents the auxiliary property predictors in our PCM. Thus, combined with the  $\epsilon(x_t, t, \theta_0)$ , it satisfies the Equation (7) in our PCM. Then, we obtain:

$$\begin{aligned} \tilde{\epsilon}(x_t, t, c_s, \mathbf{c}_p; \theta_s, \theta_p) &\approx \tilde{\epsilon}_p(x_t, t, c_s, \mathbf{c}_p; \theta_p) \\ &\quad + w_s \nabla_{x_t} \log p(x_t|t) \\ &\quad + (1-w_s) \nabla_{x_t} \log p(c_s|x_t, t) \end{aligned} \quad (17)$$

As for the term  $\nabla_{x_t} \log p(c_s|x_t, t)$ , it actually equals to  $(\nabla_{x_t} \log p(x_t|c_s, t) + \nabla_{x_t} \log p(x_t|t))$  based on the chain rule of probability for similar reasons. Besides, because the term  $\log p(x_t|t)$  already appears in the above equation with parameter  $w_s$ , we could approximate it by:

$$\nabla_{x_t} \log p(c_s|x_t, t) \approx \nabla_{x_t} \log p(x_t|c_s, t) \approx \epsilon(x_t, t, c_s).$$

Substituting this and introducing parameters  $\theta_c$  and  $\theta_0$ , we have:

$$\begin{aligned} \tilde{\epsilon}(x_t, t, c_s, \mathbf{c}_p; \theta_s, \theta_p) &\approx \tilde{\epsilon}_p(x_t, t, c_s, \mathbf{c}_p; \theta_p) \\ &\quad + w_s \nabla_{x_t} \log p(x_t|t) \\ &\quad + (1-w_s) \epsilon(x_t, t, c_s; \theta_c) \end{aligned} \quad (18)$$

$$\approx \tilde{\epsilon}_p(x_t, t, c_s, \mathbf{c}_p; \theta_p) \quad (19)$$

$$\begin{aligned} &\quad + w_s \epsilon(x_t, t) \\ &\quad + (1-w_s) \epsilon(x_t, t, c_s; \theta_c) \end{aligned} \quad (20)$$

The last two terms satisfy the Equation (3) in our SCM, leading to:

$$\tilde{\epsilon}(x_t, t, c_s, \mathbf{c}_p; \theta_s, \theta_p) \approx \tilde{\epsilon}_p(x_t, t, c_s, \mathbf{c}_p; \theta_p) + \tilde{\epsilon}_s(x_t, t, c_s; \theta_s).$$

This completes the proof.

## G: Validation Set (VS set)

The validation set includes molecules containing the following representative scaffolds: Piperazine (N1CCNCC1), Pyrimidine (c1cncn1 and c1cncn1), Pyridine (c1ccncc1), Benzene (c1cccc1), Furan (c1ccoc1), Phenol (c1cccc1O), Benzothiazole (c1ccc2ncsc2c1), Thiazole (c1escn1), and Naphthalene (c1ccc2cccc2c1). All ten scaffolds are used for GuacaMol and ZINC250K. For QM9, which does not contain molecules with Benzothiazole, Thiazole, or Naphthalene substructures, we use the remaining seven scaffolds for validation.